

Optimal Resonant Beam Charging for Electronic Vehicles in Internet of Intelligent Vehicles

Qingqing Zhang, Mingqing Liu, Xing Lin, Qingwen Liu*, Jun Wu, and Pengfei Xia

Abstract—To enable electric vehicles (EVs) to access to the internet of intelligent vehicles (IoIV), charging EVs wirelessly anytime and anywhere becomes an urgent need. The resonant beam charging (RBC) technology can provide high-power and long-range wireless energy for EVs. However, the RBC system is inefficient. To improve the RBC power transmission efficiency, the adaptive resonant beam charging (ARBC) technology was introduced. In this paper, after analyzing the modular model of the ARBC system, we obtain the closed-form formula of the end-to-end power transmission efficiency. Then, we prove that the optimal power transmission efficiency uniquely exists. Moreover, we analyze the relationships among the optimal power transmission efficiency, the source power, the output power, and the beam transmission efficiency, which provide the guidelines for the optimal ARBC system design and implementation. Hence, perpetual energy can be supplied to EVs in IoIV virtually.

Index Terms—Internet of Things, Internet of Intelligent Vehicles, Resonant Beam Charging.

I. INTRODUCTION

The fast growing mobile computing and communication applications of electric vehicles (EVs), such as electric cars, unmanned aerial vehicles (UAVs) and electromobiles, accelerate the development of the internet of intelligent vehicles (IoIV) [1], [2], [3], [4], [5], [6]. To enable the EVs to access to the IoIV anytime and anywhere, the batteries of EVs should be able to support their operations all the time [7], [8], [9]. However, refilling the EVs' batteries faces the challenges of battery capacity limitation and power supply availability. Wired charging is inconvenient, because users have to seek for a power output and wait a long time for charging. Therefore, wireless charging or wireless power transfer (WPT) attracts great attention to provide perpetual energy supplies for EVs virtually [3], [8], [10], [11].

The existing wireless charging technologies include: inductive coupling, magnetic resonance coupling, electromagnetic (EM) radiation, and resonant beam charging (RBC) [12], [13], [14]. In the RBC system, multiple devices can be charged simultaneously by one power transmitter, which is like Wi-Fi communications. Moreover, RBC can charge electrical devices with high power over a long distance [13], [15], [16]. Therefore, RBC is suitable for charging EVs. To improve RBC efficiency, the adaptive resonant beam charging (ARBC)

Q. Zhang, M. Liu, X. Lin, Q. Liu, J. Wu, and P. Xia, are with College of Electronics and Information Engineering, Tongji University, Shanghai, People's Republic of China, e-mail: anne@tongji.edu.cn, clare@tongji.edu.cn, linxing018@tongji.edu.cn, qliu@tongji.edu.cn, wujun@tongji.edu.cn, and pengfei.xia@gmail.com.

* Corresponding author.

Copyright (c) 2012 IEEE. Personal use of this material is permitted. However, permission to use this material for any other purposes must be obtained from the IEEE by sending a request to pubs-permissions@ieee.org.

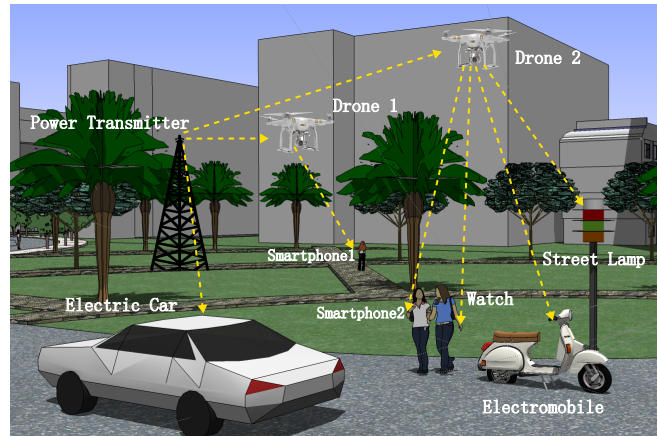


Fig. 1 Adaptive Resonant Beam Charging Applications

was presented in [17], [18]. The ARBC transmitter can adjust the source power according to the receiver preferred charging power based on feedback control. For charging a 1000mAh Li-ion battery, the ARBC system can save at least 60.4% of charging energy compared with the RBC system [17].

Fig. 1 gives an ARBC application scenario. An ARBC transmitter, which is like a base station in wireless communications, is installed to provide wireless power to devices in its coverage. The electric car, drone 1, and drone 2 are all in the transmitter's coverage, so they can be charged wirelessly. At the same time, the two drones can charge devices within their own coverage, i.e., work as relays. Drone 1 can charge smartphone 1, while drone 2 supports charging smartphone 2, watch, electromobile and street lamp simultaneously.

To demonstrate the mechanism of the ARBC system, Fig. 2 shows the ARBC system diagram [17]. The ARBC system is separated into multiple conceptually independent

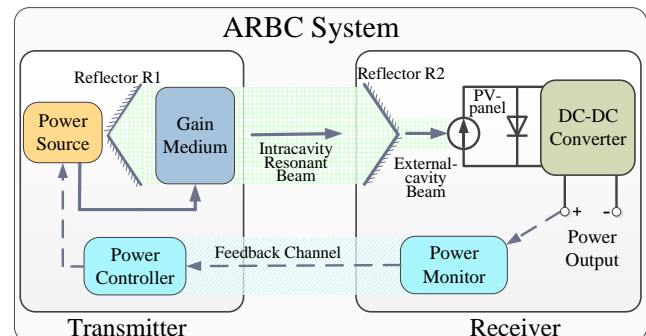


Fig. 2 Adaptive Resonant Beam Charging System Diagram

modules: 1) the electricity-to-beam conversion module: the power source provides electrical power to stimulate the gain medium under the control of the power controller, and then the intra-cavity resonant beam power can be generated. 2) the beam transmission module: the intra-cavity resonant beam travels through the air and arrives at the ARBC receiver with attenuation. 3) the beam-to-electricity conversion module: the intra-cavity resonant beam is partially transformed to the external-cavity beam, which can be converted to the electrical power by a photovoltaic-panel (PV-panel). The direct current-to-direct current (DC-DC) converter is adopted to convert the PV-panel output current and voltage to the preferred output values. 4) the feedback module: the power monitor gets the preferred output current and voltage, thus power, and sends the values back to the power controller through the feedback channel. Repeating this procedure, electric vehicles can be charged with the device preferred current and voltage.

The contributions of this paper include: 1) We prove that the optimal power transmission efficiency uniquely exists, based on the closed-form formula of the end-to-end maximum power transmission efficiency of the ARBC system; 2) We analyze the relationships among the optimal power transmission efficiency, the source power, the beam transmission efficiency, and the output power, which provide the guidelines for the optimal ARBC system design and implementation.

In the rest of this paper, we will at first discuss the ARBC system modeling. Then, we will analyze the end-to-end performance of the ARBC system. Finally, we will make a conclusion and discuss the open issues.

II. SYSTEM MODELING

In this section, we will describe the mathematical models of the ARBC system, including the electricity-to-beam conversion, the beam transmission and the beam-to-electricity conversion.

A. Electricity-to-Beam Conversion

At the ARBC transmitter, the power controller informs the power source to generate the corresponding electrical source power P_s , which can stimulate the gain medium to generate the intra-cavity resonant beam power at the transmitter P_{bt} . From [17], P_{bt} varies with different beam wavelengths. When the distance between the transmitter and the receiver is 0, the measured values of P_s and P_{bt} for the 1540-1560nm beam system can be obtained from [19]. Therefore, the relationship between P_s and P_{bt} can be described. The triangles in Fig. 3 show the measured data points for 1550nm. As can be seen, the beam power can be stimulated out only when the source power is over a certain threshold since extra power consumption caused by other factors, such as thermal effect, is inevitable.

To depict the relationship between P_{bt} and P_s when P_s is over the certain threshold quantitatively, we use the following square-root fitting method:

$$P_{bt} \approx a_1 \sqrt{b_1 + P_s} + c_1, \quad (1)$$

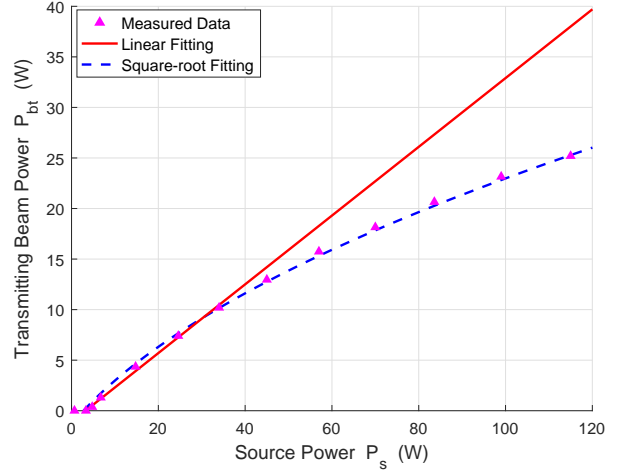


Fig. 3 Transmitting Beam Power vs. Source Power

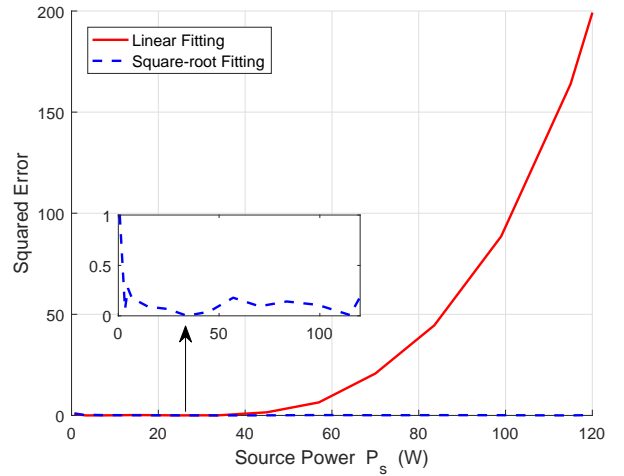


Fig. 4 Squared Error vs. Source Power

where a_1 , b_1 , and c_1 are three coefficients, which are listed in Table I.

In Fig. 3, the solid-line gives the linear curve-fitting relationship between P_{bt} and P_s , which is detailed in [17]. The dash-line shows the square-root curve-fitting relationship between P_{bt} and P_s . As can be seen, the dash-line matches the triangles very well, while the solid-line can not match the triangles when P_s is over 40W. This illustrates that the square-root approximation in (1) is more consistent with the measurements than the linear one.

To evaluate the two fitting methods, we take the squared error based on the measured data in [19] to depict the relative

TABLE I Electricity-to-Beam Conversion Parameters

| Symbol | Value |
|--------|--------|
| a_1 | 3.331 |
| b_1 | 10.2 |
| c_1 | -11.99 |

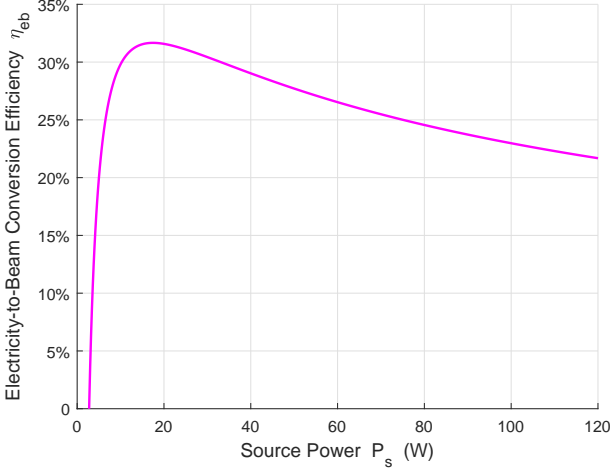


Fig. 5 Electricity-to-Beam Conversion Efficiency vs. Source Power

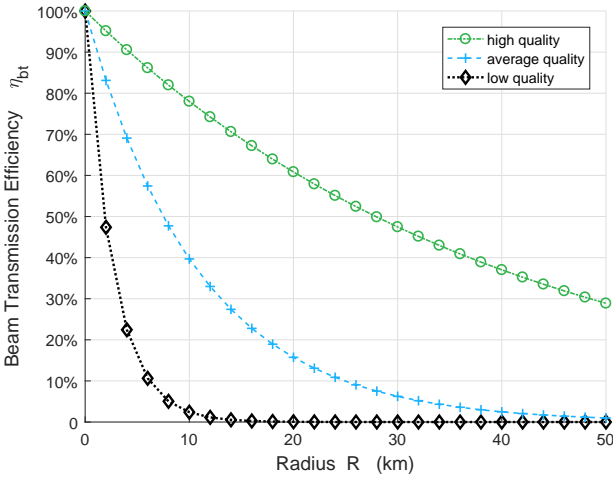


Fig. 6 Beam Transmittance Efficiency vs. Transmission Radius

deviation between the fitting values and the measured values. The squared error S_e is calculated as:

$$S_e = (P_{bt} - P_s)^2, \quad (2)$$

where P_{bt} can be the linear-fitting beam power value or the square-root fitting beam power value. Fig. 4 shows the errors of the linear-fitting method and the square-root fitting method. It can be seen that squared error of the linear-fitting method is larger than that of the square-root fitting method.

Based on the squared error, the mean square error (MSE) of the two methods can be obtained according to:

$$MSE = \frac{1}{n} \sum_{i=1}^n [P_{bt(i)} - P_{s(i)}]^2, \quad (3)$$

where n is the number of the measured data. The MSE of the linear-fitting method is 43.5967, while that of the square-root fitting method is only 0.2057. Therefore, the measured data can be better explained by the square-root fitting method rather than the linear-fitting method.

Based on (1), the electricity-to-beam conversion efficiency η_{eb} can be obtained as:

$$\eta_{eb} = \frac{P_{bt}}{P_s} \approx \frac{a_1 \sqrt{b_1 + P_s} + c_1}{P_s}. \quad (4)$$

From (4), η_{eb} relies on P_s . Fig. 5 illustrates how η_{eb} changes with P_s . When the source power P_s is over the threshold, η_{eb} starts to increase dramatically until reaching the peak. The peak value is about 31.7%. Then, η_{eb} tends to decline against the peak slightly as P_s increases.

B. Beam Transmission

After being stimulated out by the electrical power at the transmitter, the intra-cavity resonant beam transmits through the air to the receiver. During the transmission procedure, the beam power suffers from attenuation, similar to EM wave propagation power loss [20]. Without attenuation, the external beam power at the receiver P_{br} is equal to the intra-cavity resonant beam power at the transmitter P_{bt} .

The factors affecting the beam power transmission include the transmission range and the air quality [17], [21]. To quantify the attenuation, we assume that the beam diameter is a constant. This assumption could be validated by controlling aperture diameters of the transmitter and the receiver.

The beam transmission efficiency η_{bt} is modeled as [21]:

$$\eta_{bt} = \frac{P_{br}}{P_{bt}} = e^{-\frac{3.91}{\nu} \left(\frac{\lambda}{550nm} \right)^{-\chi} R}, \quad (5)$$

where ν is the atmospheric visibility, λ is the beam wavelength in nm, χ is the size distribution of the scattering particles, and R is the radius of the transmission range. For different air quality, ν and χ take different values. Here we take three typical scenarios, i.e., high visibility, average visibility, and low visibility, into consideration. For the three scenarios, χ can be specified as:

$$\chi = \begin{cases} 1.6, & \text{high visibility} & (21km \leq \nu \leq 50km) \\ 1.3, & \text{average visibility} & (6km \leq \nu \leq 21km) \\ 0.585\nu^{\frac{1}{3}}, & \text{low visibility} & (\nu \leq 6km) \end{cases} \quad (6)$$

Fig. 6 depicts the variation of η_{bt} with R under the three different scenarios when λ takes 1550nm. The parameters are given in Table II. It is clear that η_{bt} decreases exponentially with the increment of R . The beam power attenuation depends on the visibility ν , which is determined by the air quality. With the same transmission radius, high visibility brings high transmission efficiency.

C. Beam-to-Electricity Conversion

At the ARBC receiver, the PV-panel is adopted to transfer the external-cavity beam power to the electrical power. Factors influencing the beam-to-electricity conversion include the received beam power, beam wavelength, and PV-cell temperature [17], [22]. In this section, we explore how these factors influence the beam-to-electricity conversion. Results here are obtained by using the standard *solar cell* Simulink model [23].

Fig. 7 demonstrates the relationships among the PV-panel output current I_{pv} , power P_{pv} and voltage V_{pv} under different

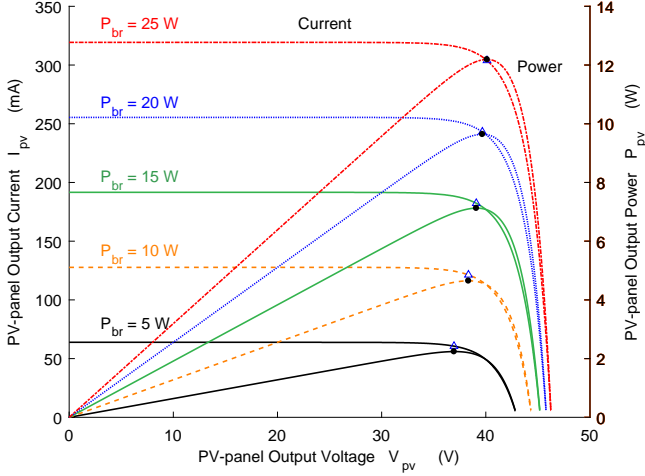


Fig. 7 PV-panel Output Current and Power vs. Voltage ($T=25^{\circ}\text{C}$)

receiver beam power P_{br} at room temperature (25°C) for the GaSb-based PV-panel with 1550nm beam. All the parameters are listed in Table III.

From Fig. 7, given P_{br} , I_{pv} keeps almost a constant when V_{pv} is below a turning point. However, when V_{pv} is over the turning point, I_{pv} drops rapidly. For the same V_{pv} , I_{pv} increases as P_{br} decreases. When I_{pv} is close to zero, V_{pv} is the open-circuit voltage, which increases as P_{br} increases. Moreover, given P_{br} , P_{pv} increases as V_{pv} increases until it reaches the peak point, which is corresponding to the turning point of I_{pv} . However, P_{pv} drops dramatically when V_{pv} is above the corresponding voltage for the peak point. For a given voltage V_{pv} , the output power P_{pv} increases when the input beam power P_{br} increases.

As to the turning point in Fig. 7, it is the maximum point of the output power, which is defined as the maximum power point (MPP). From [24], given the certain scenario and P_{br} , MPP is proved to be a unique point. For maximum efficiency, the PV-panel is supposed to work at the MPP, which can be tracked with the maximum power point tracking (MPPT) technology [25]. We define P_m as the P_{pv} corresponding to the MPP. For example, if $P_{br} = 25\text{W}$, the MPP is unique as 12.19W, and the corresponding unique I_{pv} and V_{pv} are 303.9mA and 40.11V, which are marked by the dots or triangles in Fig. 7.

On the other hand, to study the effects of the PV-cell temperature T on the beam-to-electricity power conversion, we carry out the simulation under three different temperatures (0°C , 25°C , 50°C) when $P_{br} = 25\text{W}$.

Fig. 8 depicts the variations of I_{pv} and P_{pv} on different V_{pv} . As can be seen, the I_{pv} and V_{pv} corresponding to the MPP goes down as T rises. Therefore, the MPP decreases as T increases.

Thereafter, MPPs under the three temperatures when P_{br} takes different values can be obtained. Dots in Fig. 9 show all the MPPs corresponding to different P_{br} . To explore the relationship between P_m and P_{br} , we adopt the following

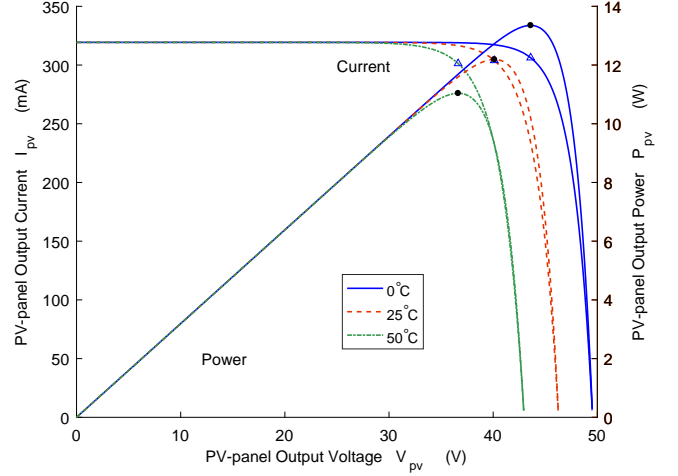


Fig. 8 PV-panel Output Current and Power vs. Voltage ($P_{br} = 25\text{W}$)

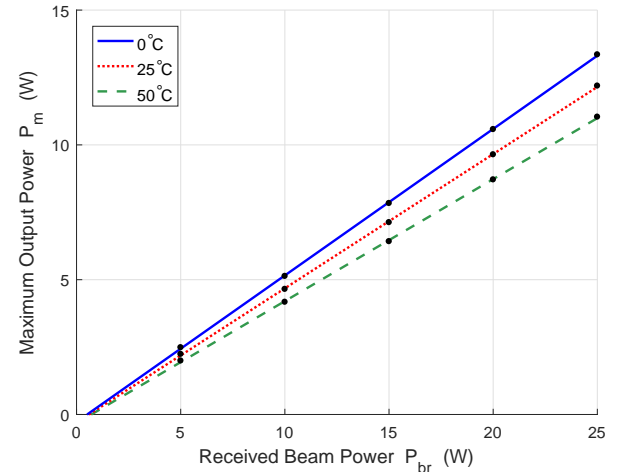


Fig. 9 Maximum Output Power vs. Received Beam Power

approximation formula:

$$P_m \approx a_2 P_{br} + b_2, \quad (7)$$

where a_2 and b_2 are the curve fitting coefficients, which are listed in Table III. As in Fig. 9, the MPP dots are all in the curves, which validates that the fitting method in (7) matches the measured MPPs well.

Thereafter, the maximum PV-panel conversion efficiency η_{bem} , that is the conversion efficiency when the PV-panel

TABLE II Beam Transmission Parameters

| Parameter | Visibility | | |
|-----------|------------|---------|--------------------------|
| | High | Average | Low |
| β | | 3.91 | |
| γ | | 550nm | |
| ν | 30km | 11km | 4km |
| χ | 1.6 | 1.3 | $0.585\nu^{\frac{1}{3}}$ |

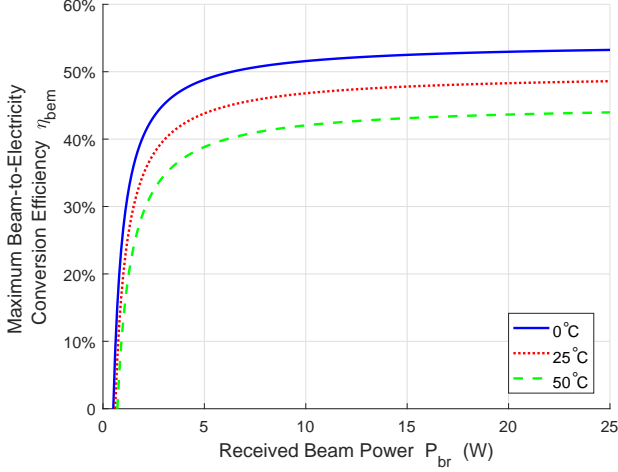


Fig. 10 Maximum Beam-to-Electricity Conversion Efficiency vs. Received Beam Power

works at the MPPs, can be depicted as:

$$\eta_{bem} = \max_{P_{pv} \rightarrow P_m} \eta_{be} = \frac{P_m}{P_{br}} = a_2 + \frac{b_2}{P_{br}}. \quad (8)$$

Fig. 10 shows how η_{bem} varies with the received beam power P_{br} . From Fig. 10, η_{bem} experiences a rapid growth at first, then it approaches to a relatively stable value. On the other hand, η_{bem} goes down with the increment of T , which is consistent with how MPPs change with T in Fig. 9.

III. END-TO-END PERFORMANCE ANALYSIS

In this section, we will at first investigate the relationship between the received beam power P_{br} and the source power P_s , i.e., the end-to-end power relationship based on the above models. Then, we will analyze the maximum end-to-end power transmission efficiency. We will prove that the optimal power transmission efficiency uniquely exists. Finally, we will discuss the guidelines of system design and implementation to achieve the optimal power transmission efficiency.

Based on (1), (5) and (7), the end-to-end power relationship can be obtained as:

$$\begin{aligned} P_m &= a_2 \eta_{bt} P_{bt} + b_2 \\ &= a_1 a_2 \eta_{bt} \sqrt{b_1 + P_s} + a_2 \eta_{bt} c_1 + b_2. \end{aligned} \quad (9)$$

As can be seen, both η_{bt} and P_s have influences on P_m . For certain η_{bt} , how P_m changes over P_s can be obtained.

Fig. 11 depicts the relationship when η_{bt} takes 100% and the PV-cell temperature T takes 0°C , 25°C and 50°C . From Fig. 11, P_m goes up gradually with the increment of P_s after reaching the power threshold for generating resonant beam. At the same time, given the certain P_s , higher P_m can be obtained when T takes smaller value.

In addition to the electricity-to-beam conversion efficiency η_{eb} , the beam transmission efficiency η_{bt} and the maximum beam-to-electricity conversion efficiency η_{bem} , the DC-DC conversion efficiency η_{dc} and the battery charging efficiency η_{ce} have impacts on the maximum overall power

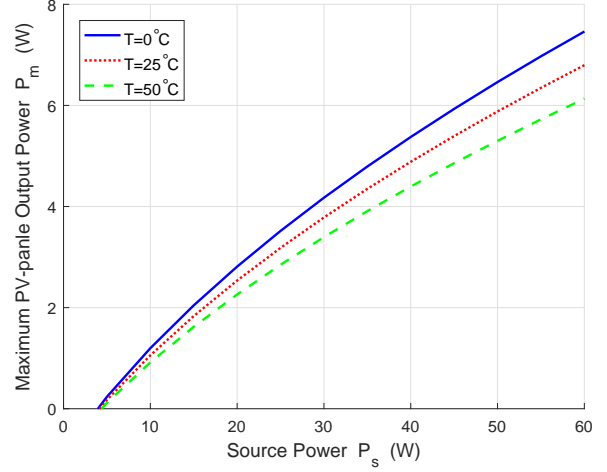


Fig. 11 Maximum Output Power vs. Source Power

transmission efficiency of the ARBC system η_{om} . η_{dc} is influenced by the DC-DC converter input power P_m and output power P_{dc} , which can be defined as:

$$\eta_{dc} = \frac{P_{dc}}{P_m}. \quad (10)$$

η_{ce} can be expressed with P_{dc} and the battery charging power as P_b , which is the ARBC system output power, as:

$$\eta_{ce} = \frac{P_b}{P_{dc}}. \quad (11)$$

All the symbols are listed in Table IV.

Based on (4), (5), (6), (8), (10) and (11), η_{om} can be modeled as:

$$\begin{aligned} \eta_{om} &= \eta_{eb} \eta_{bt} \eta_{bem} \eta_{dc} \eta_{ce} \\ &= \eta_{eb} \eta_{bt} \left(a_2 + \frac{b_2}{\eta_{eb} \eta_{bt} P_s} \right) \eta_{dc} \eta_{ce} \\ &= \frac{a_1 a_2 \eta_{bt} \sqrt{b_1 + P_s} + (a_2 c_1 \eta_{bt} + b_2)}{P_s} \eta_{dc} \eta_{ce}. \end{aligned} \quad (12)$$

From (12), η_{om} relies on P_s , η_{bt} , η_{dc} , and η_{ce} . According to [26], value of η_{dc} can be 90%. According to [27], η_{ce} can be up to 99%. In the following, we will illustrate how η_{om} varies with P_s and η_{bt} in different scenarios.

TABLE III Beam-to-Electricity Conversion Parameters

| Parameter | Symbol | Value |
|---------------------------------------|----------|-----------------------------|
| Short-circuit current | I_{sc} | 0.305A |
| Open-circuit voltage | V_{oc} | 0.464V |
| Irradiance used for measurement | I_{r0} | 2.7187W/cm ² |
| Beam frequency | γ | 1.9355×10^{14} Hz |
| Quality factor | n | 1.1 |
| Number of series cells | N | 72 |
| PV-panel material | | GaSb-based |
| Measurement temperature | T | 120°C |
| Simulation temperature | | 0°C / 25°C / 50°C |
| P_m - P_r curve fitting parameter | a_2 | 0.5434 / 0.4979 / 0.4525 |
| P_m - P_r curve fitting parameter | b_2 | -0.2761 / -0.2989 / -0.3209 |

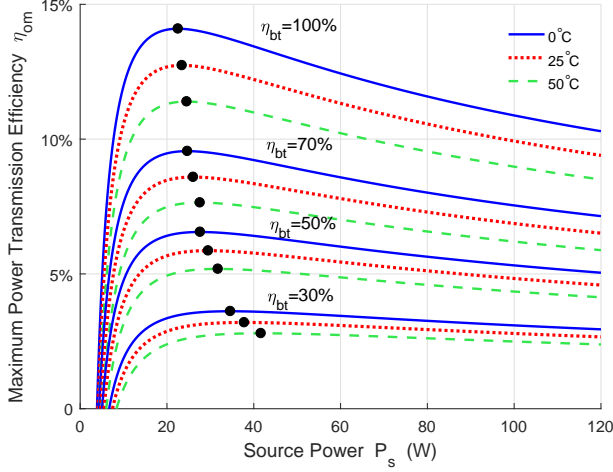


Fig. 12 Maximum Power Transmission Efficiency vs. Source Power

Fig. 12 shows the relationship between η_{om} and P_s when the beam transmission efficiency η_{bt} varies from 100% to 30% and T takes $0^\circ C$, $25^\circ C$ and $50^\circ C$. As can be seen, η_{om} climbs up rapidly with P_s increasing at first, then it goes down and takes a downward trend. Moreover, for certain η_{bt} , η_{om} takes smaller value as T increases.

Moreover, there seems to be a peak point of η_{om} for each curve in Fig. 12. To verify its existence and uniqueness when η_{bt} takes a certain value and the variable P_s lies in the interval $(0, +\infty)$, we take the derivation of η_{om} with respect to P_s as:

$$\begin{aligned}
 & \frac{d\eta_{om}}{dP_s} \\
 &= \left[a_2\eta_{bt} \frac{a_1P_s/(2\sqrt{b_1+P_s}) - (a_1\sqrt{b_1+P_s} + c_1)}{P_s^2} - \frac{b_2}{P_s^2} \right] \eta_{dc}\eta_{ce} \\
 &= \frac{a_2\eta_{bt}\eta_{dc}\eta_{ce}}{P_s^2\sqrt{b_1+P_s}} \left[\frac{a_1P_s}{2} - a_1(b_1+P_s) - (c_1 + \frac{b_2}{a_2\eta_{bt}})\sqrt{b_1+P_s} \right] \\
 &= \frac{a_2\eta_{bt}\eta_{dc}\eta_{ce}}{(t^2 - b_1)^2 t} \left[-\frac{a_1}{2}t^2 - (c_1 + \frac{b_2}{a_2\eta_{bt}})t - \frac{a_1b_1}{2} \right] \\
 & \quad (\text{where } t = \sqrt{b_1+P_s}) \\
 & := \frac{a_2\eta_{bt}\eta_{dc}\eta_{ce}}{(t^2 - b_1)^2 t} g(t), \tag{13}
 \end{aligned}$$

where $g(t) = -a_1t^2/2 - (c_1 + b_2/(a_2\eta_{bt}))t - a_1b_1/2$ is a quadratic function. So, the sign of the derivation depends on the function $g(t)$.

We define $g(\sqrt{b_1}) = -a_1b_1 - (c_1 + b_2/(a_2\eta_{bt}))\sqrt{b_1}$. With the help of MATLAB, we find $g(\sqrt{b_1}) > 0$ for all the cases. Moreover, we have $g(+\infty) = -\infty$ and $g(0) = -a_1b_1/2 < 0$, since a_1 and b_1 are both greater than 0 in all the considered scenarios. By the well-known intermediate value theorem, there exists one and only one point $\xi \in (\sqrt{b_1}, +\infty)$ that $g(\xi) = 0$. Thus, when $t \in (\sqrt{b_1}, \xi)$, η_{om} is strictly increasing, and when $t \in (\xi, +\infty)$, η_{om} is strictly decreasing. Therefore, η_{om} has a unique maximum value as P_s changes.

Dots in Fig. 12 are the optimal points of η_{om} . To maximize the overall efficiency of the ARBC system, the system should work at the source power point corresponding to the optimal η_{om} . However, there are some cases where

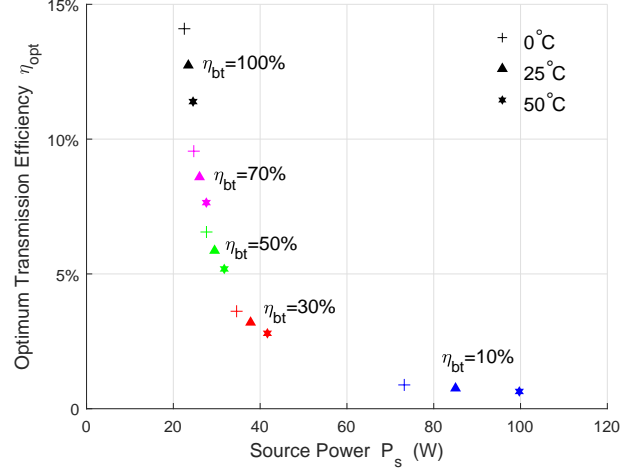


Fig. 13 Optimal Transmission Efficiency vs. Source Power

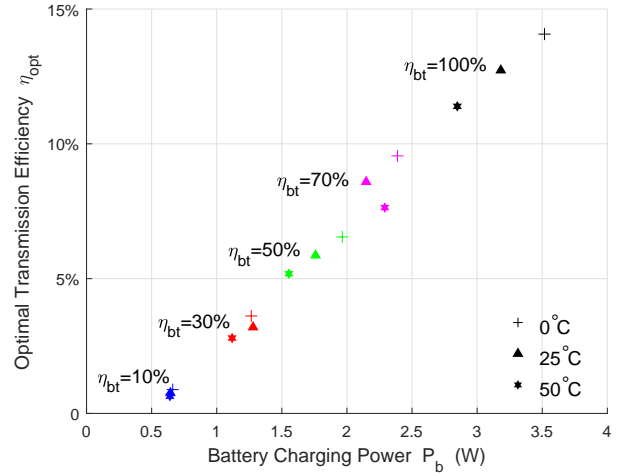


Fig. 14 Optimal Transmission Efficiency vs. Battery Charging Power

P_s is strictly required, while the requirement for η_{om} is not so urgent. Therefore, the unique optimal maximum power transmission efficiency point provides grounds for compromise between the source power and the overall efficiency.

We take η_{opt} as the optimal maximum power transmission efficiency. Then, we can get how η_{opt} changes over P_s when T takes $0^\circ C$, $25^\circ C$, $50^\circ C$ and η_{bt} varies from 0 to 100%. Fig. 13 gives the relationships. As can be seen, for

TABLE IV Transmission or Conversion Efficiency

| Parameter | Symbol |
|---|--------------|
| Electricity-to-beam conversion efficiency | η_{eb} |
| Beam transmission efficiency | η_{bt} |
| Beam-to-electricity conversion efficiency | η_{be} |
| DC-DC conversion efficiency | η_{dc} |
| Battery charging efficiency | η_{ce} |
| Maximum power transmission efficiency | η_{om} |
| Optimal maximum power transmission efficiency | η_{opt} |

certain T , η_{opt} decreases dramatically from the maximum point as P_s increases and η_{bt} decreases at the beginning. Then, the decreasing trend of η_{opt} becomes slow. If with the same η_{bt} , η_{opt} takes lower value when T increases, and P_s corresponding to the η_{opt} becomes larger. At the same time, for certain η_{bt} , T has less impacts on η_{opt} as P_s goes up.

Fig. 13 provides the guidelines for source power control, so that the optimal charging efficiency can be selected to fully utilize the transmitter energy under a certain PV-cell temperature. For example, in a military application scenario, to guarantee the sensors working long enough time, batteries should be charged in time before running out. Since charging the batteries with wires is hard to implement in the military fighting environment, wireless charging becomes urgent. Sending an unmanned aerial vehicle (UAV) which carries the power source to charge the sensors can be an ideal option. To guarantee all the sensors as much energy as possible from the UAV, the UAV should charge the sensors with the optimal maximum transmission efficiency η_{opt} . Here we assume that the sensors take all the power the UAV offers regardless of the current or voltage. According to Fig. 13, if under same T , η_{opt} is determined by η_{bt} , which is influenced by the air quality and the distance between the power supplier and the sensor. Then, under the certain air quality, the UAV can control P_s provided to the sensor to maximize the source power with η_{opt} .

Fig. 14 shows how the optimal transmission efficiency η_{opt} changes over the battery charging power P_b . From it high P_b brings high η_{opt} with the increment of η_{bt} under same T . Meanwhile, for the certain η_{bt} , the impacts that T has on η_{opt} are much larger when P_b takes bigger value. While, if with same η_{bt} , high η_{opt} tends to be obtained at lower temperature. As is known, different vehicles have different types of batteries, and each battery has its characteristic which determines different charging power requirements. To utilize the output energy with maximum efficiency, if η_{bt} is given, the battery type can then be determined with reference to Fig. 14.

From Figs. 12, 13 and 14, the influencing factors, which include the air quality and the transmission radius, can be summarized as the beam transmission efficiency η_{bt} . To analyze the relationship between η_{opt} and η_{bt} at different T , Fig. 15 is given. High η_{bt} guarantees high η_{opt} . Though with slightly bend, η_{opt} and η_{bt} takes approximately a linear relationship. At the same time, if with same η_{bt} , η_{opt} is much higher when T takes lower value.

Therefore, the maximum power transmission efficiency η_{om} is influenced by the source power P_s , the beam transmission efficiency η_{bt} , and the PV-cell temperature T . The relationships among the three are shown in Fig. 16. If P_s and η_{bt} are given, η_{om} can be obtained directly. For example, when P_s is 40W and the η_{bt} is 70%, the η_{om} is about 9%.

In summary, the factors influencing the overall ARBC efficiency include the source power, the beam wavelength, the air quality, the transmission radius, the PV-cell temperature, the efficiency of DC-DC and the battery charging efficiency. We obtain the following information from the above analysis:

- We derive the closed-formed maximum ARBC power transmission efficiency η_{om} .

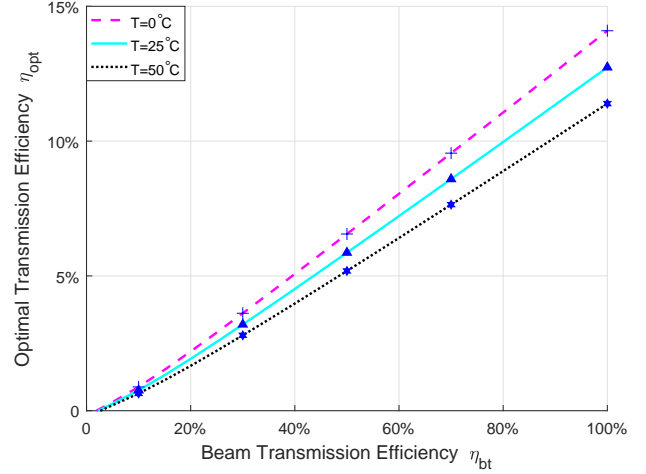


Fig. 15 Optimal Transmission Efficiency vs. Beam Transmission Efficiency

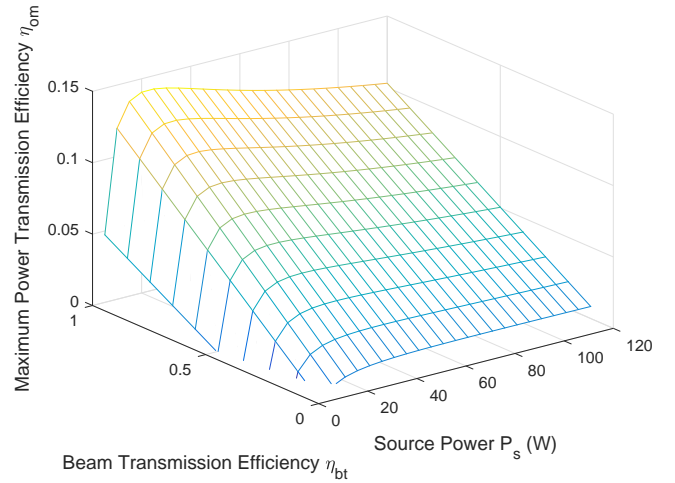


Fig. 16 Maximum Power Transmission Efficiency vs. Beam Transmission Efficiency and Source Power ($T=0^\circ\text{C}$)

- We prove that the optimal value of η_{om} , i.e., the optimal end-to-end transmission efficiency η_{opt} , uniquely exists as P_s changes.
- We analyze the relationships among η_{opt} , P_s , P_b , and η_{bt} under different circumstances, which provide design and development guidelines for the ARBC system.

IV. CONCLUSIONS

In this paper, we present a multi-module analytical model of the adaptive resonant beam charging system for electric vehicles (EVs) in the internet of intelligent vehicles (IoIV). Based on the real measurements, the quadratic curve-fitting function is adopted for the electricity-to-beam power conversion. Thus, the closed-form formula of the end-to-end power transmission efficiency is obtained. Moreover, we prove that the optimal power transmission efficiency uniquely exists. After analyzing the optimal power transmission efficiency based on the source power, the output power, and the beam transmission efficiency, the design and implementation guide-

lines to optimize the end-to-end power transmission efficiency are provided.

There are some open issues to be studied for future work. For example:

- The electricity-to-beam conversion study in this paper is limited by the measured data availability. Thus, investigating the expanded power range is worth to pursue in the future.
- To enable EVs to access to the IoIV anytime and anywhere, different battery types should be investigated. The research on the characteristics of different batteries is necessary to optimize the battery charging performance.

REFERENCES

- [1] M. Hua, C. Li, Y. Huang, and L. Yang, "Throughput maximization for UAV-enabled wireless power transfer in relaying system," in *2017 9th International Conf. on Wireless Communications and Signal Processing (WCSP)*, Nanjing, China, Oct. 11-13, 2017.
- [2] Q. Meng and J. Jin, "The terminal design of the energy self-sufficiency Internet of Things," in *2011 International Conf. on Control, Automation and Systems Engineering (CASE)*, Singapore, Singapore, July 30-31, 2011.
- [3] R. Zhang, X. Cheng, and L. Yang, "Flexible energy management protocol for cooperative EV-to-EV charging," *IEEE Trans. Intell. Transp. Syst.*, vol. 31, no. 3, pp. 97–101, May 2016.
- [4] F. Zeng, R. Zhang, X. Cheng, and L. Yang, "Channel prediction based scheduling for data dissemination in VANETs," *IEEE Communications Letters*, vol. 21, no. 6, pp. 1409–1412, June 2017.
- [5] X. Cheng, C. Chen, W. Zhang, and Y. Yang, "5G-enabled cooperative intelligent vehicular (5Genciv) framework: When benz meets marconi," *IEEE Intell. Syst.*, vol. 32, no. 3, pp. 53–59, May 2017.
- [6] X. Cheng, L. Yang, and X. Shen, "D2D for intelligent transportation systems: A feasibility study," *IEEE Trans. Intell. Transp. Syst.*, vol. 16, no. 4, pp. 1784–1793, Aug. 2015.
- [7] X. Cheng, X. Hu, L. Yang, K. I. I. Husain, P. Krein, R. Lefevre, Y. Li, H. Nishi, J. G. Taiber, F. Wang, Y. Zha, W. Gao, and Z. Li, "Electrified vehicles and the smart grid: The ITS perspective," *IEEE Trans. Intell. Transp. Syst.*, vol. 15, no. 4, pp. 1388–1404, June 2014.
- [8] X. Cheng, R. Zhang, and L. Yang, "Consumer-centered energy system for electric vehicles and the smart grid," *IEEE Intell. Syst.*, vol. 31, no. 3, pp. 97–101, May 2016.
- [9] R. Zhang, X. Cheng, and L. Yang, "Energy management framework for electric vehicles in the smart grid: A three-party game," *IEEE Commun. Mag.*, vol. 54, no. 12, pp. 93–101, Dec. 2016.
- [10] T. Yasuda, "Proposal of the passive type dynamic wireless power transfer system for EVs," in *2017 19th European Conf. on Power Electronics and Applications (EPE'17 ECCE Europe)*, Warsaw, Poland, Sept. 11-14 2017.
- [11] B. Feng, H. Zhang, H. Zhou, and S. Yu, "Locator/Identifier split networking: A promising future internet architecture," *Commun. Surveys Tuts.*, vol. 19, no. 4, pp. 2927–2948, July 2017.
- [12] X. Lu, D. Niyato, P. Wang, D. I. Kim, and Z. Han, "Wireless charger networking for mobile devices: Fundamentals, standards, and applications," *IEEE Wireless Communications*, vol. 22, no. 2, pp. 126–135, Apr. 2015.
- [13] Q. Liu, J. Wu, P. Xia, S. Zhao, W. Chen, Y. Yang, and L. Hanzo, "Charging unplugged: Will distributed laser charging for mobile wireless power transfer work?" *IEEE Vehicular Technology Magazine*, vol. 11, no. 4, pp. 36–45, Dec. 2016.
- [14] Q. Zhang, W. Fang, Q. Liu, J. Wu, P. Xia, and L. Yang, "Distributed laser charging: A wireless power transfer approach," *IEEE Internet Things J.*, June to appear, 2018, doi: 10.1109/JIOT.2018.2851070.
- [15] R. Della-Pergola, O. Alpert, O. Nahmias, and V. Vaisleib, "Spatiality distributed laser resonator," Israel Patent 14/125 984, May, 2014.
- [16] O. R. Mor, O. Alpert, A. Slepoy, L. Golan, R. Sagi, V. Shmukler, E. Ronen, O. Nahmias, and V. Vaisleib, "System for optical wireless power supply," Israel Patent 15/484 722, Sept., 2017.
- [17] Q. Zhang, X. Shi, Q. Liu, J. Wu, P. Xia, and Y. Liao, "Adaptive distributed laser charging for efficient wireless power transfer," in *2017 IEEE 86th Vehicular Technology Conference (VTC-Fall)*, Toronto, Canada, Sept. 24-27, 2017.
- [18] Q. Zhang, W. Fang, M. Xiong, Q. Liu, J. Wu, and P. Xia, "Adaptive resonant beam charging for intelligent wireless power transfer," *IEEE Internet Things J.*, Aug. to appear, 2018, doi: 10.1109/JIOT.2018.2867457.
- [19] L. D. S. Seminex, "Laser diode source - 1550nm," [Online]. Available: <https://www.laserdiodesource.com/laser-diode-product-page/1470nm-1532nm-1550nm-50W-multi-chip-fiber-coupled-module-Seminex>, July 2017.
- [20] H. Weichel, *Laser beam propagation in the atmosphere*, 1st ed., Washington: SPIE press, 1990.
- [21] O. Karatay, "An alternative approach to free space optical communication link," Master's thesis, İzmir Institute of Technology, July 2004.
- [22] M. S. Aziz, S. Ahmad, I. Husnain, A. Hassan, and U. Saleem, "Simulation and experimental investigation of the characteristics of a PV-harvester under different conditions," in *2014 International Conf. on Energy Systems and Policies (ICESP)*, Islamabad, Pakistan, Nov. 24-26 2014, pp. 1–8.
- [23] T. Salmi, M. Bouzguenda, A. Gastli, and A. Masmoudi, "MATLAB/Simulink based modeling of photovoltaic cell," *International Journal of Renewable Energy Research (IJRER)*, vol. 2, no. 2, pp. 213–218, Feb. 2012.
- [24] S. Liu and R. A. Dougal, "Dynamic multiphysics model for solar array," *IEEE Power Eng. Rev.*, vol. 22, no. 5, p. 66, May 2002.
- [25] M. A. G. de Brito, L. Galotto, L. P. Sampaio, G. de A. e Melo, and C. A. Canesin, "Evaluation of the main MPPT techniques for photovoltaic applications," *IEEE Trans. Ind. Electron.*, vol. 60, no. 3, pp. 1156–1167, Mar. 2013.
- [26] L. G. Salem, J. G. Louie, and P. P. Mercier, "A flying-domain DC-DC converter powering a Cortex-M0 processor with 90.8% efficiency," in *2016 IEEE International Solid-State Circuits Conference (ISSCC)*, San Francisco, USA, Jan. 31-Feb. 4, 2016.
- [27] J. W. Stevens and G. P. Corey, "A study of lead-acid battery efficiency near top-of-charge and the impact on PV system design," in *Conference Record of the Twenty Fifth IEEE Photovoltaic Specialists Conference - 1996*, Washington, USA, May 13-17, 1996.